Astron. Astrophys. 360, 777–788 (2000)

ASTRONOMY AND ASTROPHYSICS

Experimental determination of scattering matrices of olivine and Allende meteorite particles

O. Muñoz[1,2], **H. Volten**[1], **J.F. de Haan**[1], **W. Vassen**[1], **and J.W. Hovenier**[1,3]

[1] Department of Physics and Astronomy, Free University, De Boelelaan 1081, 1081 HV Amsterdam, The Netherlands
[2] Instituto de Astrofísica de Andalucía, CSIC, P.O. Box 3004, 18080 Granada, Spain
[3] Astronomical Institute "Anton Pannekoek", University of Amsterdam, Kruislaan 403, 1098 SJ Amsterdam, The Netherlands

Received 15 March 2000 / Accepted 31 May 2000

Abstract. We have measured the scattering matrix as a function of the scattering angle of randomly oriented particles of a Mg-rich olivine sample and a ground piece of Allende meteorite as cometary analogues using lasers at two wavelengths (442 nm and 633 nm). The elements of the scattering matrix, F_{ij}, depend on the scattering angle, the wavelength of the laser light, and on the size, shape and refractive index of the particles. The sample of olivine has been prepared so that four different size distributions were obtained, and results for these size distributions are presented. The element ratio $-F_{12}/F_{11}$, which in our case equals the degree of linear polarization for unpolarized incident light, is of particular interest, since it can be compared directly with observations e.g. for comets and asteroids. This ratio shows negative values at angles close to the backward direction for Allende meteorite and olivine particles at both wavelengths. Such negative polarization has been observed for many objects in the solar system. Our data have been compared with polarization data of comets and asteroids. We conclude that differences in the maximum polarization observed for different comets can be due to differences in the size distributions and/or the color of cometary dust particles.

Key words: polarization – scattering – comets: general

1. Introduction

Understanding the formation of the solar system has been a main goal for astrophysicists and geophysicists for many years. To study in detail processes of planet formation in the very early stage of the solar system, investigation of old solar system material plays a key role. The study of such material is accelerating lately with the development of new space programs such us the NASA $Stardust$ mission and the European Space Agency (ESA) Rosetta mission. The $Stardust$ NASA space mission started with the launch of a spacecraft in February 1999. It will fly close to the comet Wild2 and bring cometary material back to Earth. ESA will start the Rosetta mission in 2003 which will visit the comet Wirtanen. This mission will concentrate on the $in\ situ$ investigation of cometary matter from the surface and the coma. The orbiter will carry a lander to the nucleus and deploy it on the surface.

The majority of meteorites are fragments from previously formed so-called planetesimals, situated in the then developing solar system in the region between Mars and the giant planets. The most primitive meteorites, carbonaceous chondrites, have an overall chemical composition similar to that of the Sun and were never severely metamorphosed or chemically altered during the history of the solar system (see e.g. Beatty & Chaikin 1990). These meteorites represent unique material for the investigation of the solar system as a whole.

Irregular dust particles play an important role in the study of comets and asteroids. The spectacular display of a bright comet is mostly caused by a cloud of micrometer-sized dust particles. This dust originates from a central source of ices and dust (the nucleus). Upon sublimation of the ices, the dust is entrained in the gas stream leaving the nucleus. From the similarity of the solar spectrum compared to that of a dusty comet, it was recognized that the light from a comet is mostly scattered sunlight. Measurements of the brightness and polarization of this light can give information on the nature of these dust particles. Differences in the polarization data of different comets have been noticed through both remote and $in\ situ$ polarization observations (e.g. Chernova et al. 1993; Levasseur-Regourd et al. 1996, 1999a; Kiselev 1999). These differences in polarization suggest differences in the physical properties of cometary dust particles.

Scattering properties of spherical particles can be calculated from Mie theory (Mie 1908), but the scattering properties of nonspherical particles can differ dramatically from those of volume- or surface- equivalent spheres. On the other hand, an exact solution for the scattering of light by nonspherical dust particles, covering all sizes and shapes that occur in nature does not exist. We refer to the book by Mishchenko et al. (2000), for a detailed description of the advantages and constraints of the often used numerical codes for light scattering by nonspherical particles. Therefore, an experimental study of the scattering behavior of irregular dust particles that are candidates for cometary material is of main importance in order to interpret space- and ground-based observations. Only a small number

Send offprint requests to: O. Muñoz
Correspondence to: Instituto de Astrofísica de Andalucía
(olga@iaa.es)

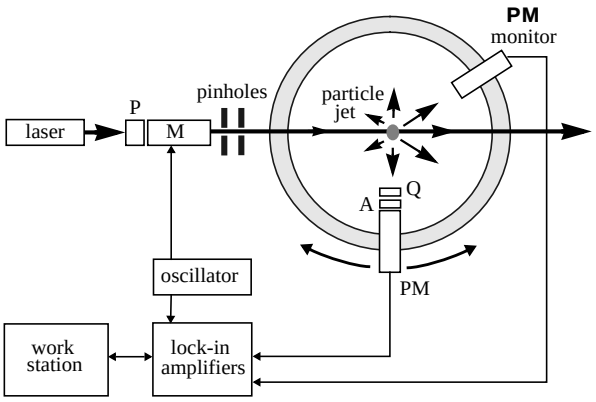

Fig. 1. Schematic picture of the experimental setup; P, polarizer; A, polarization analyzer; Q, quarter-wave plate; PM, photomultiplier; M electro-optic modulator.

of results of laboratory measurements have been published. Microwave measurements require manufacturing centimeter-sized scattering objects with the desired shape and refractive index, studying the scattered microwave beam for this object, and transforming the results to other wavelengths by keeping the ratio size/wavelength fixed (Gustafson 2000). A disadvantage of such measurements is that they can be performed only for one particle size, shape and orientation at a time. Another approach is to work at visible wavelengths by letting a beam of laser light be scattered by a single particle (Weiss-Wrana 1983) or an ensemble of particles falling through the beam. The latter method has been used by several authors to establish the angular distribution of all elements of the scattering matrix (e.g. Holland & Gagne 1970; Perry et al. 1978; Kuik et al. 1991; Volten et al. 2000) or only the phase function and the degree of linear polarization for incident unpolarized light as a function of the scattering angle (Jaggard et al. 1981; West et al. 1997). Polarization phase curves for clouds of dust particles under microgravity conditions have been obtained recently (Worms et al. 1999).

Since mid- and far-infrared spectra have provided strong evidence for the presence of crystalline Mg-rich olivine in comets (Campins & Ryan 1989; Hanner et al. 1994; Colangeli et al. 1995; Kolokolova & Jockers 1997; Brucato et al. 1999), we have measured the whole scattering matrix as a function of the scattering angle of randomly oriented particles of a natural Mg-rich olivine sample and a ground piece of Allende meteorite as cometary analogues. The measurements have been carried out with lasers at two different wavelengths, 442 and 633 nm.

Laboratory measurements can be used in two different ways; 1) directly for interpreting optical observations of brightness and polarization of astronomical objects with dust, such as comets and asteroids, or 2) indirectly, by fitting the measured values to results of calculations by varying the size and shape (e.g. spheroids, cylinders, Gaussian random shapes) of the particles until a good fit has been obtained. The resulting particle properties, i.e. size and shape, can be used for computations of radiative properties at an arbitrary wavelength in the visible and infrared part of the spectrum for which the refractive index is known. The laboratory measurements presented in this work have been used in a direct way, by comparing them with observational data of comets and asteroids obtained by other authors (e.g. Dollfus 1989; Levasseur-Regourd et al. 1996, 1999a). In this way, we have derived some physical characteristics of dust particles in comets and asteroids.

A review of the theory involved in these experiments and a description of the experimental setup used to measure the scattering matrix elements are presented in Sect. 2. In Sect. 3, the samples are characterized. Results of our experiments are presented and discussed in Sect. 4. Conclusions are given in Sect. 5.

2. Some concepts of light scattering and the experimental setup

In this section, we summarize some concepts from light scattering theory that are used in this work. The flux and polarization of a quasi-monochromatic beam of light can be represented by a column vector $\mathbf{I} = \{I, Q, U, V\}$, or Stokes vector (Van de Hulst 1957; Hovenier & van der Mee 1983), where I is proportional to the total flux of the beam. The Stokes parameters Q and U represent differences between two components of the flux for which the electric field vectors oscillate in mutual orthogonal directions. The Stokes parameter V is the difference between two oppositely circularly polarized components of the flux. A plane through the direction of propagation of the beam is chosen as a plane of reference for the Stokes parameters.

If light is scattered by an ensemble of randomly oriented particles and time reciprocity applies, as is the case in our experiment, the Stokes vectors of the incident beam and the scattered beam are related by a 4×4 scattering matrix, for each scattering angle θ, as follows (Van de Hulst 1957, Sect. 5.22),

$$\begin{pmatrix} I_s \\ Q_s \\ U_s \\ V_s \end{pmatrix} = \frac{\lambda^2}{4\pi^2 D^2} \begin{pmatrix} F_{11} & F_{12} & F_{13} & F_{14} \\ F_{12} & F_{22} & F_{23} & F_{24} \\ -F_{13} & -F_{23} & F_{33} & F_{34} \\ F_{14} & F_{24} & -F_{34} & F_{44} \end{pmatrix} \begin{pmatrix} I_i \\ Q_i \\ U_i \\ V_i \end{pmatrix} \quad (1)$$

where the subscripts i and s refer to the incident and scattered beam, respectively, λ is the wavelength of the incident beam and D is the distance from the ensemble to the detector. The matrix with elements F_{ij} is called the scattering matrix. Its elements depend on the scattering angle, but not on the azimuthal angle. Here the plane of reference is the scattering plane, i.e., the plane containing the incident and the scattered light. The elements F_{ij} contain information about the size distribution, shape and refractive index of the scatterers. It follows from Eq. (1) that there are 10 different matrix elements to be determined. This number is further reduced in case a scattering sample consists of randomly oriented particles with equal amounts of particles and their mirror particles. In that case, the four elements $F_{13}(\theta)$, $F_{14}(\theta)$, $F_{23}(\theta)$, and $F_{24}(\theta)$ are identically zero over the entire angle range (Van de Hulst 1957).

A schematic picture of the experimental setup used to measure the scattering matrix is shown in Fig. 1. We use either a HeNe laser (633 nm, 5mW) or a HeCd laser (442 nm, 40mW)

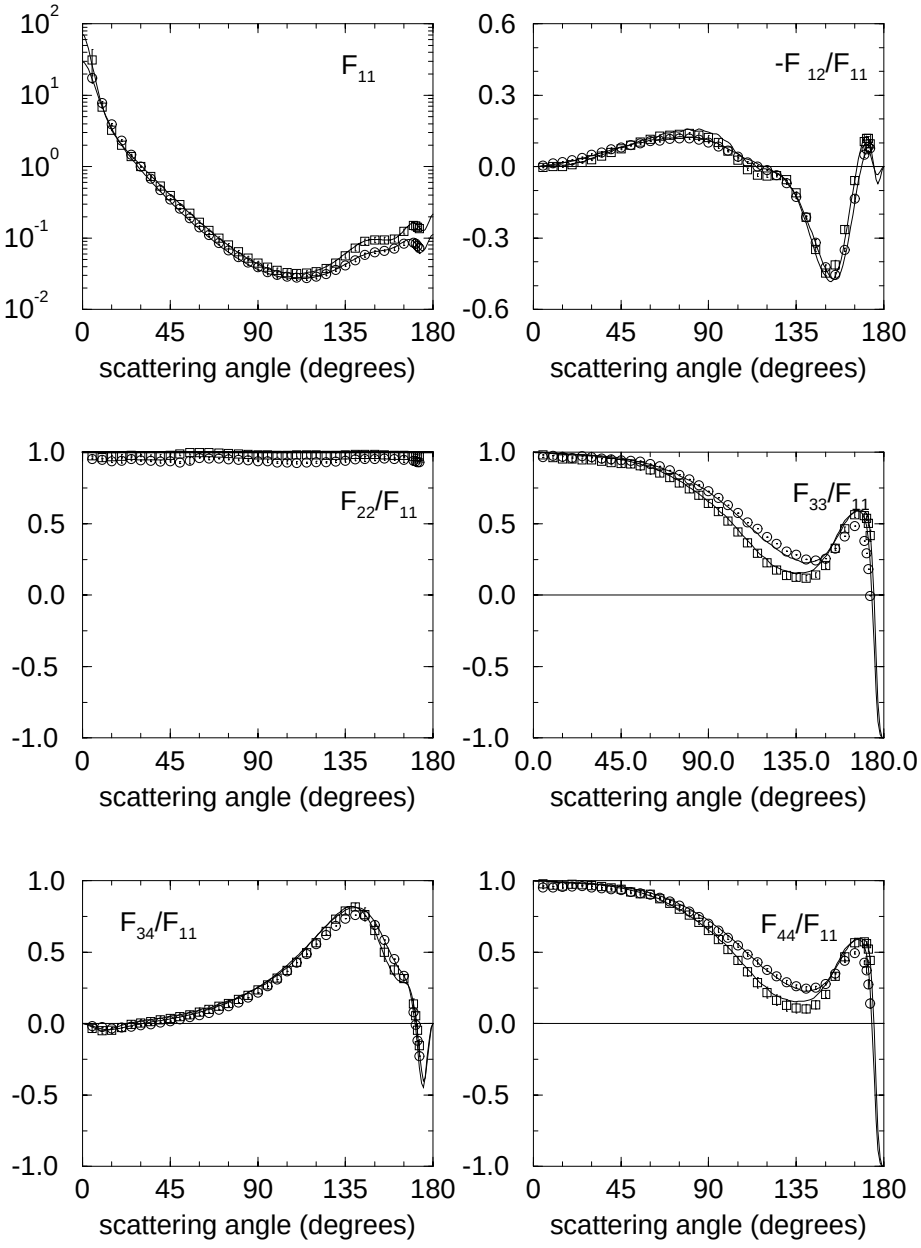

Fig. 2. Calibration measurements with water droplets. The squares correspond to the measurements at 442 nm and the circles to the results at 633 nm. The measurements are presented together with their error bars. In case no error bars are shown, they are smaller than the symbols. The solid lines correspond to the Mie calculations at both wavelengths.

as a light source. The laser light passes through a polarizer oriented at an angle γ_P and an electro-optic modulator oriented at an angle γ_M (angles of optical elements are the angles between their optical axes and the scattering plane, measured counterclockwise when looking in the direction of propagating of the light). The modulated light is subsequently scattered by the ensemble of randomly oriented particles located in a jet stream produced by an aerosol generator. The scattered light passes through a quarter-wave plate oriented at an angle γ_Q and an analyzer oriented at an angle γ_A (both optional) and is detected by a photomultiplier tube which moves along a ring. A range in scattering angles is covered from approximately 5 (nearly forward scattering) to about 173 (nearly backward scattering). We employ polarization modulation in combination with lock-in detection to obtain all elements of the four-by-four scattering matrix up to a common constant. A more detailed description of the setup is given by Hovenier (2000).

Errors in the measured matrix elements originate from fluctuations in the measured signal or signals. For each data point at a given scattering angle, 720 measurements are conducted in about 2 seconds. The values obtained for the measured matrix elements or combinations of matrix elements are the average of several data points (about 5 or more) and the corresponding experimental error is the standard deviation in these. The resulting standard deviations are indicated by error bars in Fig. 2 and later figures. When no error bar is shown the value for the standard deviation is smaller than the symbol plotted. A monitor photomultiplier at a fixed scattering angle (see Fig. 1) is used to correct for variations in the amount of particles in the jet stream during the measurement run.

We investigated the reliability of the measurements presented in this paper by applying the Cloude coherency test (Hovenier & van der Mee 1996). For the particles of the ground piece of Allende meteorite, we had not enough sample material to measure $F_{13}(\theta)$ and $F_{23}(\theta)$. To be able to apply the Cloude coherency test for these samples, we assumed these elements to be zero at all scattering angles, since they proved to be zero within the experimental errors for the other samples. We found that for all matrix elements, the values measured for scattering angles from 5 to 173 are in agreement with the Cloude coherency test within the experimental errors.

Measurements with water droplets have been done in order to test the alignment of the set-up. Since the water droplets have spherical shapes, we could compare the experimental results with those obtained from Mie calculations. The water droplets were produced by a nebulizer. For convenience, we normalize all matrix elements (except F_{11} itself) to F_{11}, i.e., we consider F_{ij}/F_{11}, with i, j = 1 to 4. Instead of F_{12}/F_{11} we have plotted the degree of linear polarization for incident unpolarized light,

$$-F_{12}/F_{11} = \frac{I_r - I_l}{I_r + I_l} = P \quad (2)$$

where I_r and I_l represent the flux of the scattered light polarized perpendicular and parallel to the plane of scattering respectively. The results of all $F_{11}(\theta)$ measurements and calculations presented are plotted on a logarithmic scale. We chose to normalize F_{11} so that it equals 1 at $\theta = 30$. We omitted the four element ratios $F_{13}(\theta)/F_{11}(\theta)$, $F_{14}(\theta)/F_{11}(\theta)$, $F_{23}(\theta)/F_{11}(\theta)$ and $F_{24}(\theta)/F_{11}(\theta)$, since we verified that these ratios do not differ from zero by more than the error bars.

A comparison between measurements with water droplets at 442 and 663 nm and Mie calculations is shown in Fig. 2. We find that there is an excellent agreement over the entire angle range measured for all scattering matrix elements. For the Mie calculations we used a log-normal size distribution (Hansen & Travis 1974) with $r_{\rm eff}$ = 1.1 μm, $v_{\rm eff}$ = 0.3, and a refractive index $m = 1.33 - i0.00$. Values for $r_{\rm eff}$ and $v_{\rm eff}$ were chosen so that the differences between the results of Mie calculations and measurements were minimized for all scattering matrix elements. Remaining differences between the measured and calculated values may be due to small aligment errors or to the fact that the size distribution of the droplets deviates somewhat from a log-normal distribution.

3. Characterization of the samples

In this section, we discuss physical characteristics of our samples of small particles (magnesium rich olivine and a ground piece of Allende meteorite), in particular their chemical composition, size distribution, complex refractive index and morphological characterization.

3.1. Olivine

The olivine was obtained from a Norwegian dunite rock with a composition of $Mg_{1.85}Fe_{0.14}SiO_4$. In Table 1, we present the chemical composition of the rock. The original rock was prepared so that the measurements could be repeated for different size distributions. The sample was ball milled and first sieved with a 125 μm sieve. The portion of the sample that passed through the sieve (particles smaller than 125 μm in diameter) was subsequently sieved in water through a sieve of 65 μm. Again the smallest particles (smaller than 65 μm) were subsequently sieved through a sieve of 20 μm. In such a way we produced four different size distributions designated as XL ($65 \leq d \leq 125\,\mu$m), L ($20 \leq d \leq 65\,\mu$m), M ($d \leq 65\,\mu$m) and S ($d \leq 20\,\mu$m), where d is the diameter of the sieving grid.

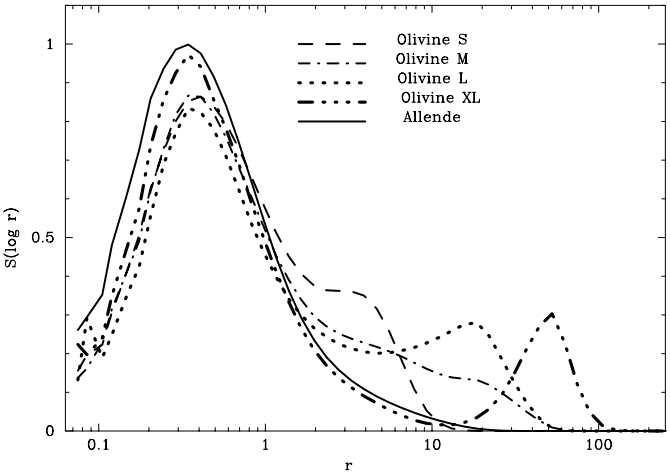

Fig. 3. Projected surface area distribution of the four olivine samples and the ground piece of Allende meteorite as a function of the radius in micrometers on a logarithmic scale.

3.2. Allende meteorite

The group of carbonaceous chondrite meteorites, type III (Mason 1971) to which the Allende meteorite belongs, has a composition close to that of the Sun (see e.g. Beatty & Chaikin 1990). The only exception relates to volatile elements. Hydrogen, carbon, nitrogen, oxygen and the noble gases are so volatile, or form compounds so volatile, that they are incapable of condensing in the inner solar system. This supports the theory that the carbonaceous chondrite meteorites condensed from the primitive solar nebula and have undergone little subsequent chemical modification. In Table 1 we present results of chemical analyses of this type of meteorites.

3.3. Particle sizes

The projected surface area distributions of projected surface equivalent spheres have been measured by using a Fritsch laser particle sizer (Konert & Vandenberghe 1997). The results for olivine samples S, M, L and XL and for the Allende meteorite particles are presented in Fig. 3, showing the projected surface distributions S(log$r$) as a function of log$r$. Here, r is the radius of a sphere having the same projected surface area as the irregular particle has, and S(log$r$)dlog$r$ gives the relative contribution

by spheres with radii in the size range [log$r$; log$r$+dlog$r$] to the total projected surface per unit volume of space. Since for irregular particles larger than about 1 μm, the projected surface area is proportional to the scattering cross section (Hodkinson 1963), Fig. 3 gives us information about how particles of different size contribute to the scattering. According to these measurements the sieving procedure did not remove all particles with diameters smaller than 65 μm from sample XL nor particles with diameters smaller than 20 μm from sample L.

Values of the effective radius ($r_{\rm eff}$) and variance ($v_{\rm eff}$) of each sample are given in Table 2. These two parameters are defined as follows:

$$r_{\rm eff} = \frac{\int_0^\infty r\pi r^2 n(r)dr}{\int_0^\infty \pi r^2 n(r)dr} \quad (3)$$

$$v_{\rm eff} = \frac{\int_0^\infty (r - r_{\rm eff})^2 \pi r^2 n(r)dr}{r_{\rm eff}^2 \int_0^\infty \pi r^2 n(r)dr} \quad (4)$$

where r is the radius and $n(r)$ is the size distribution of projected surface equivalent spheres (Hansen & Travis 1974). Values of $n(r)$ were derived from the measured projected surface distributions.

Since the olivine samples XL and L show bi-modal projected surface distributions, the $r_{\rm eff}$ and $v_{\rm eff}$ that are used to characterize them are only a first order indication of the size of the particles.

3.4. Refractive indices

The exact values of the refractive indices of our samples are unknown. According to the measured optical constants of different types of silicates published so far (e.g. Jäger et al. 1994; Dorschner et al. 1995), the imaginary part of the refractive index, k, of iron-poor silicates is very low (of the order of 10^{-4} in the visible range). However, the absorption increases by increasing the amount of iron in the sample being higher at 442 nm than at 633 nm. Since the amount of iron in our olivine sample is quite low we expect low values of the imaginary part of the refractive index. In contrast, the amount of iron in the Allende sample is much higher than for olivine (see Table 1), so we can expect a higher imaginary part of the refractive index. This is something we can easily establish by looking at the sample: the color of the Allende sample is dark grey, whereas the olivine sample is light green.

3.5. Morphology

The morphological characterization was done by using a field emission Scanning Electron Microscope (SEM). In Fig. 4, we present SEM photographs of our samples of olivine and Allende meteorite particles. Since the four olivine samples have been produced by milling and sieving from the same original rock, we do not expect significant differences in the shape of the particles of the different olivine samples. Indeed, we see quite similar shapes for all of the olivine samples shown in Fig. 4. The shape of the particles of the Allende meteorite (Fig. 4.e), is very similar to that of the olivine samples. Therefore, the possible effect of differences in shape on the scattering behavior of these five samples has not been taken into account in the discussion of the measurements (Sect. 4).

Table 1. Chemical analyses (in % by weight) of our Olivine sample and Carbonaceous chondrite meteorite type III, which is the group to which Allende meteorite belongs (Mason 1971).

Component	Olivine	C. Chondrite III
FeS	-	6.74
SiO_2	41	33.40
Fe_2O_3	7	-
TiO_2	-	0.10
Al_2O_3	0.5	2.51
Cr_2O_3	0.4	0.52
FeO	-	25.43
MnO	0.1	0.19
MgO	49	23.98
CaO	0.05	2.56
Na_2O	-	0.51
K_2O	-	0.04
P_2O_5	-	0.38
H_2O	-	2.07
C	-	0.47
NiO	0.035	1.64
CoO	-	0.08

Table 2. Overview of the properties of the samples studied.

Sample	$r_{\rm eff}$ (m)	$v_{\rm eff}$	sieves used	color
Olivine XL	6.3	6.8	65 < d 125 m	light green
Olivine L	3.8	3.7	20 < d 65 m	light green
Olivine M	2.6	5.0	d 65 m	light green
Olivine S	1.3	1.8	d 20 m	light green
Allende	0.8	3.3	–	dark grey

4. Results and discussion

In Sect. 4.1, we present the measured scattering matrices as functions of the scattering angle for the samples studied. We compare the experimental results for the different samples in Sect. 4.2. Furthermore, the measured angular distributions of the degree of linear polarization for unpolarized incident light is compared with observational data of comets and asteroids in Sect. 4.3.

4.1. Measurements

In Figs. 5 and 6, we present the complete scattering matrices for the Allende meteorite particles (stars) and the olivine samples XL (circles), L (squares), M (diamonds), and S (triangles) at 442 nm and 633 nm, respectively. We refrained from showing the element ratios $F_{13}(\theta)/F_{11}(\theta)$, $F_{14}(\theta)/F_{11}(\theta)$, $F_{23}(\theta)/F_{11}(\theta)$ and $F_{24}(\theta)/F_{11}(\theta)$, since they were found to be zero over the entire range of scattering angles within the accuracy of the measurements. This is in agreement with the as-

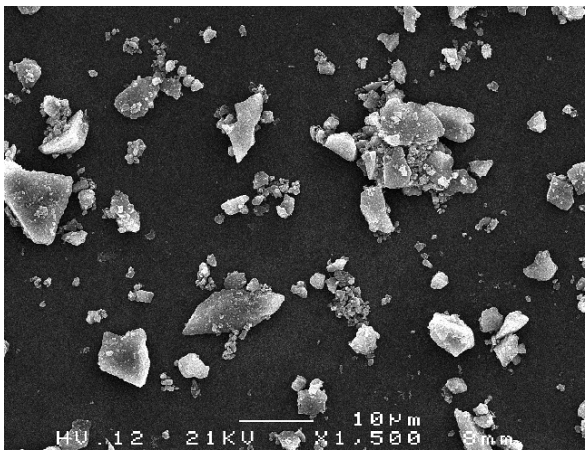

a.1

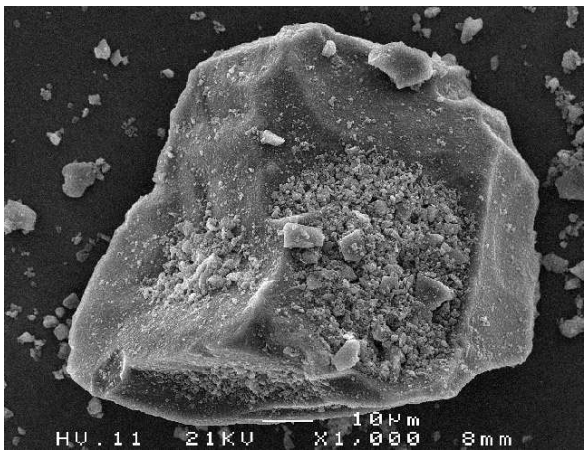

a.2

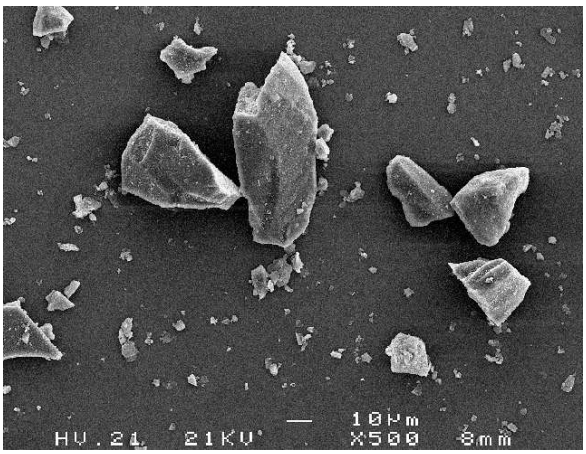

b

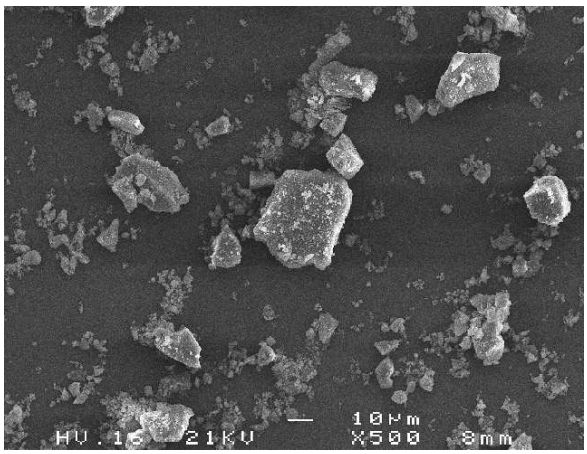

c

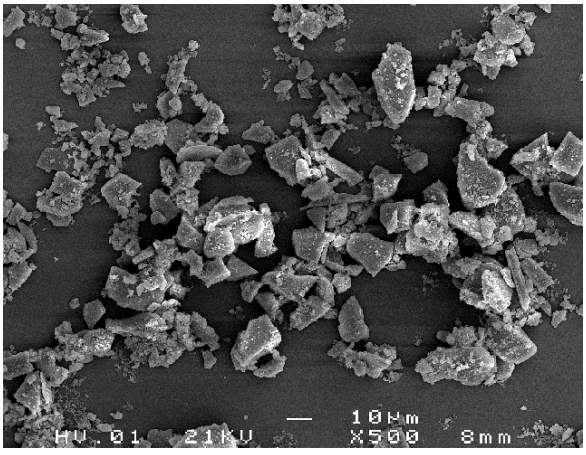

d

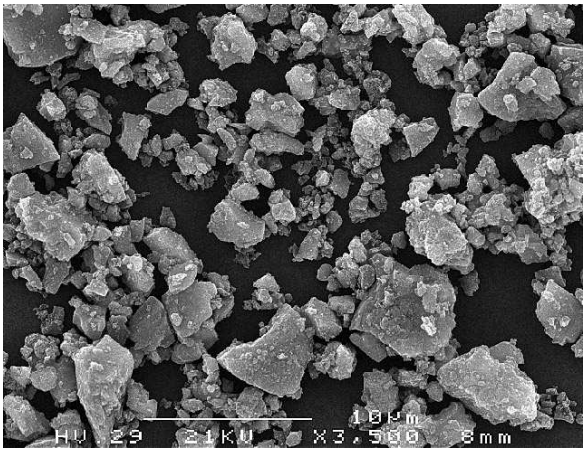

e

Fig. 4a–e. SEM photographs of olivine samples **X L** (**a.1** and **a.2**), **L b**, **M c**, **S d** and Allende meteorite **e**. In each photograph the white bar denotes 10 m.

Table 3. Steepness of $\mathbf{F}_{11}$

	(nm)	**XL**	**L**	**M**	**S**	Allende
Steepness	442	130	114	131	170	255
	633	104	101	132	180	122

sumption of randomly oriented particles with equal amounts of particles and their mirror particles (Van de Hulst 1957). Clearly, Eq. (2) is valid for our samples. The $scattering\ function$ or $phase\ function$ ($F_{11}(\theta)$) is shown on a logarithmic scale and normalized to 1 at 30 degrees. The measurements for olivine sample XL show larger error bars than the measurements for the other samples. This is predominantly due to the fact that the particles in sample XL are relatively large so that relatively few particles are present in the scattering volume during the measurements, thereby decreasing the signal-to-noise ratio. An increase in the jet flow would have improved the accuracy, but this was not possible because of the limited amount of sample material available.

In all cases the $scattering\ functions$, $F_{11}(\theta)$, are smooth functions of the scattering angle showing a strong forward peak; they are featureless and flat at side scattering angles and have almost no structure at back-scattering angles. This behavior seems to be a general property of ensembles of natural mineral particles (Jaggard et al. 1981; West et al. 1997; Volten et al. 2000). Looking in more detail, we see some differences between the four olivine samples. Although the shapes of the curves are similar their steepnesses (see Table 3), defined as the measured maximum of $F_{11}(\theta)$ divided by its measured minimum, over the scattering angle range of 5 to 173 , are different. The smallest value of the steepness at both wavelengths is presented by olivine sample L. In contrast, the Allende meteorite sample (which consists of the smallest particles) exhibits the largest steepness at 442 nm, while its value at 633 nm is quite low. This indicates that the complex refractive index strongly influences the steepness, because for Allende meteorite we expect a larger imaginary part of the refractive index due to the high percentage of iron in the sample (see Sect. 3.4).

The measured $-F_{12}(\theta)/F_{11}(\theta)$ curves show only minor differences for the four olivine samples (XL, L, M and S) at 442 nm. However, at 633 nm more pronounced differences occur and the highest maximum values are obtained for olivine samples M and S. We will discuss the results for this function in more detail in Sect. 4.3.

The $F_{22}(\theta)/F_{11}(\theta)$ ratios are often used as a measure for the nonsphericity of the particles, since for spheres this function is equal to 1 at all scattering angles. In all the samples we have studied in this work, this ratio decreases from almost 1 at angles close to the forward direction to a minimum at side-scattering, and increases again at back-scattering angles (Figs. 5 and 6).

We also observe that $F_{33}(\theta)/F_{11}(\theta) \neq F_{44}(\theta)/F_{11}(\theta)$ at all scattering angles, with $F_{44}(\theta)/F_{11}(\theta) > F_{33}(\theta)/F_{11}(\theta)$ at back-scattering angles (Figs. 5 and 6). This seems to be a general trend for nonspherical particles (Mishchenko et al. 2000).

The general pattern of $F_{34}(\theta)/F_{11}(\theta)$ is the same for all the samples with a broad side-scattering maximum separating two negative branches at small and large scattering angles.

4.2. Comparison of different samples

In Figs. 5 and 6, we see that the measurements for olivine samples M and S (diamonds and triangles respectively) yield nearly the same functions at both wavelengths. If we compare the results of $F_{22}(\theta)/F_{11}(\theta)$ and $F_{44}(\theta)/F_{11}(\theta)$ for these two samples (M and S) with those for the other two olivine samples (XL and L) we see large differences. For these ratios of scattering matrix elements, samples S and M exhibit larger values at most scattering angles than the other two olivine samples. Indeed, when looking at the values for $r_{\rm eff}$ in Table 2, it is surprising that samples S and M show such a similar scattering behavior while samples L and M, that show a similar difference in $r_{\rm eff}$ values, differ highly in scattering behavior.

Another interesting feature is that for almost all scattering angles the lowest values for $F_{22}(\theta)/F_{11}(\theta)$ and $F_{44}(\theta)/F_{11}(\theta)$ occur for olivine sample L. Since sample L is intermediate in size (see Table 2), we do not a priori expect this sample to show this extreme behavior. It is remarkable that the XL sample, while having the largest $r_{\rm eff}$, presents scattering behavior that is intermediate with respect to L and M. The reason might be that $v_{\rm eff}$ is larger for sample XL than for L, so that the small particles in sample XL contribute more to the total scattering than those in sample L. The projected surface distributions shown in Fig. 3 support this argument.

4.3. Measured degree of linear polarization compared with data for comets and asteroids

In Fig. 7, we compare $-F_{12}(\theta)/F_{11}(\theta)$ at 442 nm and 633 nm for olivine sample S (left panel) and for the Allende meteorite (right panel). The measured $-F_{12}(\theta)/F_{11}(\theta)$ at scattering angles between about 45 and 145 for the olivine sample is higher at 633 nm than at 442 nm. However, for the Allende sample, the $-F_{12}(\theta)/F_{11}(\theta)$ curves are quite similar at both wavelengths and at almost all scattering angles. The behavior of the maximum of $-F_{12}(\theta)/F_{11}(\theta)$ for irregular particles may be clarified along the following lines.

We first consider some rules that are based on limiting cases for very small particles and very large particles. For very small particles (sizes smaller than or approximately equal to the wavelength) the maximum polarization tends to decrease with the size parameter, and, therefore, increase with wavelength if the refractive index m is constant (Yanamandra-Fisher & Hanner 1999; Mishchenko et al. 2000). For very large particles (sizes much larger than the wavelength) we assume that geometric optics holds. Then, the behavior of the maximum polarization as a function of wavelength will depend on the product of the absorption coefficient, a, and the average diameter, d, of the particles, because this product determines the contribution of internally reflected light to the scattered light. If the product ad is small, many internal reflections occur which will lower the

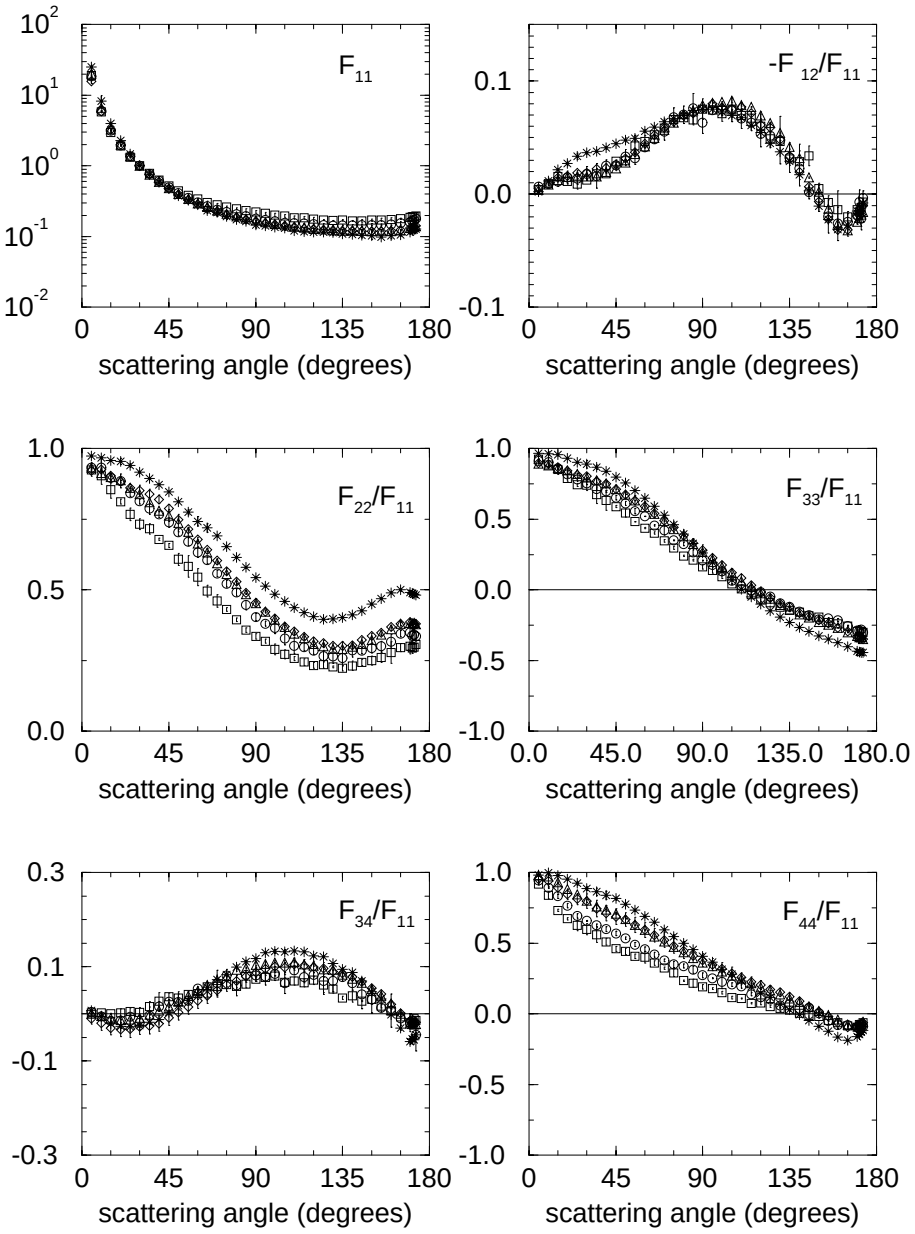

Fig. 5. Measured scattering matrix elements as a function of the scattering angle for Allende meteorite (stars) and olivine samples **XL** (circles), **L** (squares), **M** (diamonds) and **S** (triangles) at 442 nm. The measurements are presented together with their error bars. In case no error bars are shown, they are smaller than the symbols.

maximum degree of polarization. The absorption coefficient is related to the imaginary part of the refractive index, k, and the wavelength, λ, as follows.

$$a = \frac{4\pi k}{\lambda} \tag{5}$$

For the olivine particles, which have a low iron content, k is small and many internal reflections are expected for all particles that have large radii in Fig. 3. In contrast, the Allende particles have a high iron content and the value of k is higher, particularly at 442 nm. It then depends on the ratio of d and λ how strongly internal reflections will contribute to the scattered light. This illustrates that, even in the limit of geometric optics, it is difficult to predict what will happen with the maximum degree of polarization as a function of wavelength and/or size, in particular since k itself is a function of wavelength.

Fig. 3 suggests that most of the scattering by olivine and Allende particles originates from small particles, because their projected surface area is relatively large. However, very small particles are inefficient scatterers, which makes it difficult to estimate precisely the relative contribution of small, intermediate and large particles to the total scattering. Here small particles refer to Rayleigh-like behavior and large particles refer to particles that show geometric-optics-like behavior.

These considerations lead to the conclusion that we cannot fully interpret the results of the measurements. For such an interpretation theoretical calculations using advanced methods that yield scattering matrices of irregular mineral particles for small, intermediate, and large particles are required. Such calculations, if at all possible, are beyond the scope of this paper. However, some clarifications seem possible, based on the rules that hold for the limiting cases and were mentioned above.